International Journal of Disaster Risk Reduction 143 (2026) 106310

Contents lists available at ScienceDirect

International Journal of Disaster Risk Reduction

journal homepage: www.elsevier.com/locate/ijdrr

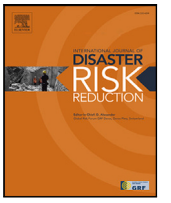

Vector-valued fragility surfaces conditioned on mainshock-aftershock intensity levels for masonry buildings

Filippo Landi [a], Giada Bartolini [b,*], Giacomo Sevieri [c], Marco Baiguera [d]

[a] Department of Civil and Industrial Engineering, University of Pisa, Largo Lucio Lazzarino, 1, Pisa, 56122, Italy
[b] Department of Civil and Environmental Engineering, University of Strathclyde, Montrose Street, 75, Glasgow, G1 1XJ, UK
[c] Aon Reinsurance Solutions, Via Calindri, 6, Milan, 20143, Italy
[d] Global Earthquake Model (GEM) Foundation, Via Ferrata, 1, Pavia, 27100, Italy

ARTICLE INFO

Keywords:
Fragility functions
Seismic sequences
Earthquake risk assessment
Masonry

ABSTRACT

Recent earthquakes have shown the devastating impact of successive ground motions on unreinforced masonry (URM) buildings. While post-earthquake surveys provide valuable insights into the seismic performance of common construction typologies, they rarely capture damage progression induced by each event, as little or no time is available for inspection between seismic sequences. As a result, most existing vulnerability models, typically based on single mainshock (MS) analyses, underestimate the effects of cumulative damage. To address this limitation, this paper proposes a new methodology that adapts the Cloud Capacity Spectrum Method for prototype URM structures modeled using a macro-element approach based on the equivalent frame idealization. A set of physically consistent mainshock–aftershock ground motion pairs is employed to perform sequential non-linear static analyses and derive fragility surfaces directly as a function of the two events, without assuming a predefined MS-induced damage state. The resulting bivariate vulnerability surface highlights the significant amplification of expected losses due to aftershocks, even following moderate MSs. The method, demonstrated on a benchmark building and validated through a consistency check against equivalent-SDOF non-linear time history analyses, is computationally efficient and readily extendable to building portfolios.

1. Introduction

The catastrophic impacts of recent seismic events have underscored the grave risks posed by earthquake sequences in highly active tectonic regions, especially when multiple high-magnitude events strike within short time intervals preventing the restoration of structural capacity between shocks [1]. The 2023 Turkiye–Syria earthquake sequence is a stark example, with the Kahramanmaraş sequence beginning with a magnitude 7.8 moment event followed nine hours later by a magnitude 7.5 earthquake and accompanied by more than 48 aftershocks (ASs) with Mw $\geq$ 5.0, [2], and tragically resulted in the loss of over 45,000 lives and an estimated 91 billion USD in economic losses over a vast area [3]. According to the Turkish Ministry of Environment and Urbanization, which carried out an extensive damage assessments on over 2.4 million buildings within the 18 impacted provinces in November 2023, the earthquakes led to the collapse of approximately 38,500 buildings, left 20,500 structures on the brink of failure, and caused heavy damage to nearly 205,000 additional buildings [4]. Similar patterns have been observed in other regions, such as the 2010–2011 Christchurch sequence in New Zealand and the 2016 Central Italy sequence, where successive events significantly exacerbated damage, particularly in unreinforced masonry (URM) buildings [5–7].

* Corresponding author.
E-mail address: giada.bartolini@strath.ac.uk (G. Bartolini).

https://doi.org/10.1016/j.ijdrr.2026.106310
Received 17 February 2026; Received in revised form 8 July 2026; Accepted 10 July 2026
Available online 16 July 2026
2212-4209/© 2026 The Authors. Published by Elsevier Ltd. This is an open access article under the CC BY-NC license (http://creativecommons.org/licenses/by-nc/4.0/).

The 2010–2011 Christchurch earthquake sequences for example, inflicted extensive damage throughout New Zealand's Canterbury region, where ASs exacerbated damage initially caused by primary events and caused severe damage even in reinforced concrete RC buildings [5]. Likewise, the Central Italy earthquake sequence began on August 24, 2016, with a 6.1 moment magnitude event, followed by two additional earthquakes of magnitudes 5.9 and 6.5 [6], resulted in severe destruction and considerable loss of life in Amatrice and surrounding historical towns and villages, with hundreds of buildings, especially URM structures, severely damaged or collapsed [7].

Those events highlight that the earthquake that causes the highest ground motion intensity at a specific site does not always correspond to the one with the highest magnitude [8]. This aspect is particularly relevant in the context of earthquake sequences, where the event generating the highest local intensity at a given site may not coincide with the mainshock (MS), but can instead occur during a subsequent AS due to spatial variability in ground motion and source-to-site effects [9]. As a result, structures that have already experienced damage during an initial event may be subjected to additional significant seismic demand during later shocks, even if these are associated with lower magnitudes. This highlights that structural damage is governed not only by the characteristics of a single event, but also by the cumulative effect of multiple ground motions acting on a progressively degrading system [10]. Despite this evidence, current seismic risk assessment methods often do not account for cumulative damage from earthquake sequences. Probabilistic Seismic Hazard Analysis (PSHA), the backbone of many regulatory frameworks, is usually based on declustered earthquake catalogs and assumes a Poissonian occurrence model that excludes foreshocks and ASs [11]. Consequently, classical fragility curves are derived based on isolated MSs and assume an undamaged building state at the onset of shaking. This assumption neglects the reality that many structures sustain initial damage during a MS, thereby altering their capacity to resist a subsequent AS.

Recent research has highlighted the importance of state-dependent fragility functions, which estimate the probability of exceeding a damage state (DS) given the intensity measure (IM) of the AS and the damage sustained during the MS [12], sometimes also considering damage accumulation within a given MS–AS sequence and across multiple sequences [13]. State-dependent fragility functions therefore, offer a more realistic representation of seismic vulnerability in regions affected by earthquake sequences. Several methodologies have been proposed to develop state-dependent fragility functions, many of which rely on non-linear dynamic analysis using multi-degree-of-freedom (MDOF) structural models. These include extensions of the Incremental Dynamic Analysis (IDA) framework to account for AS sequences [14], as well as Cloud Analysis approaches using unscaled ground motions [15–17]. While robust, these methods are computationally demanding.

Simplified procedures based on non-linear static pushover analysis have also gained traction as computationally efficient alternatives to non-linear dynamic approaches for deriving fragility relationships under seismic sequences. In these methods, the effects of the MS are typically represented through modifications of the structural capacity curve, allowing the response of a pre-damaged structure to subsequent seismic events to be estimated without explicitly performing consecutive non-linear dynamic analyses. For example, Polese et al. [18,19], and Pedone et al. [20] developed state-dependent fragility functions by applying capacity reduction factors to simulate MS-induced damage. In particular, Polese et al. developed such functions through the Incremental N2 (IN2) method, while Pedone et al. through the Cloud Capacity Spectrum Method (CCSM), employed to evaluate the structure's performance in both undamaged and damaged states, while accounting for record-to-record variability [21]. While significant progress has been made in assessing RC structures [14] and, within certain limits related to specific case studies, timber structures [22], the seismic fragility of masonry buildings under sequential earthquake scenarios remains comparatively less explored. Recent studies have highlighted the importance of explicitly accounting for cumulative damage effects in URM buildings subjected to earthquake sequences. For instance, [23] proposed a damage-state-dependent framework based on consecutive non-linear dynamic analyses and energy-based damage indices, showing that conventional approaches neglecting cumulative damage may significantly underestimate seismic risk for URM structures.

At the same time, recent research has introduced vector-valued or bivariate fragility formulations to explicitly characterize earthquake sequences through coupled MS–AS intensity measures. For example, [24] proposed a framework for deriving MS–AS fragility surfaces for RC structures using separate IMs for MSs and ASs, while accounting for cumulative damage through the Park–Ang damage index. More recently, [25] developed machine-learning-based fragility surfaces for RC frame buildings subjected to MS–AS sequences, demonstrating the feasibility of efficient prediction of joint exceedance probabilities across IMs. These studies highlighted the advantages of fragility surfaces over conventional scalar formulations in capturing cumulative sequence effects. However, these applications have mainly focused on RC structures and computationally intensive non-linear dynamic analyses. Studies explicitly addressing masonry buildings under earthquake sequences remain limited and are generally based on state-dependent formulations requiring the definition of intermediate DSs and the execution of consecutive non-linear dynamic analyses. One of the few examples addressing damage to masonry structures due to clustered seismicity is the already mentioned work by Inarritu et al. [23], where the authors perform consecutive non-linear dynamic analyses accounting for damage accumulation by applying the methodology proposed in [26] to develop state-dependent fragility curves for some URM buildings. However, simplified and computationally efficient vector-valued approaches for masonry structures subjected to MS–AS sequences are still largely unavailable in the literature.

The need for efficient methodologies for assessing the vulnerability of masonry structures under earthquake sequences is particularly relevant in Europe, where a large proportion of the built heritage consists of masonry buildings—for example, approximately 57% of residential buildings in Italy are masonry structures [27]. In parallel, the field of catastrophe modeling is evolving to incorporate multi-hazard and cascading events, including earthquake sequences [28], aligning with the growing interest in natural catastrophe risk assessment in the insurance and reinsurance sectors [29]. However, fundamental questions about how seismic sequences affect structural vulnerability, especially for URM structures, remain open.

Table 1
Benchmark mechanical parameters.

Young's modulus	Shear modulus	Specific weight	Compressive strength	Shear strength
1750 MPa	550 MPa	21 kN/m^3	3.2 MPa	0.065 MPa

Building upon recent developments in vector-valued fragility formulations for seismic sequences, this paper proposes a procedure for deriving vector-valued fragility and vulnerability functions for URM structures subjected to MS–AS seismic sequences based on non-linear static analysis. Unlike the more common state-dependent approaches found in the literature – mainly developed for RC structures [20,30] – which require the a priori definition of a MS-induced DS, the proposed method enables the assessment of building fragility and vulnerability due to seismic sequences through computationally efficient multivariate functions. In particular, the fragility and vulnerability of URM buildings subjected to MS–AS sequences are investigated through newly proposed fragility and vulnerability surfaces defined in terms of coupled MS and AS intensity levels. Section 2 introduces the proposed methodology, including the selected IM and ground motion set, the procedure for non-linear static analysis, and the evaluation of performance points for MSs and ASs, as well as the derivation of vector-valued fragility and vulnerability surfaces conditioned on MS and AS intensity levels. Section 3 presents the results for a benchmark structure representative of a typical Mediterranean residential building [31], used to quantify the effect of seismic sequences through the proposed approach. Finally, conclusions are drawn in Section 4.

2. Material and methods

This section presents the methodology adopted to derive vector-valued fragility and vulnerability surfaces conditioned on MS–AS intensity levels for URM buildings. First, the benchmark masonry structure used to illustrate the application of the methodology is introduced. Second, the selection of the intensity measure and engineering demand parameter (EDP) considered in the study are discussed, together with the associated assumptions and limitations. Next, the ground-motion selection and scaling procedure employed to construct the MS–AS record set is described. Subsequently, the non-linear static analysis framework and the software module used for the pushover analyses are introduced. Finally, the following subsections describe the main steps of the proposed procedure, including: (i) non-linear static analysis of the undamaged structure; (ii) evaluation of the performance points under MS and AS spectra; (iii) derivation of the bivariate fragility functions; and (iv) construction of the vector-valued fragility and vulnerability surfaces conditioned on MS and AS intensity levels.

2.1. Benchmark structure

The proposed methodology will be presented in the following subsections with reference to the benchmark URM building firstly introduced by [32] and adopted to assess masonry modeling strategies in [31]. The main characteristics of the building, including its geometry, structural configuration, and the masonry mechanical properties are briefly recalled here. Complementary input data, presented in the original document, are provided as supplementary material in [31].

The three-story masonry building, 11.3 m high, is a typical example of existing Mediterranean and Central European units and is characterized by a rectangular layout, 8.5 m × 10 m in plan. The building is characterized by English bond solid clay brick walls bonded with lime mortar. The external walls at ground and first floor are 0.55 m thick, while all the remaining walls are 0.45 m thick. The floors are flexible timber floors (dead load 1.0 kN/m^2 and live load 2 kN/m^2) while the double slope roof consists of a timber structure with rafters supported by joists. The assumed dead load of the roof was 1.25 kN/m^2. The relevant masonry mechanical properties are reported in Table 1, while the plan layout of the shear-resistant walls and the 3D model of the structure is shown in Fig. 1.

2.2. Engineering demand parameter selection

In probabilistic seismic risk assessment, structural damage is commonly described through fragility relationships expressing the probability of reaching or exceeding a given DS conditioned on the seismic IM [33]. Within earthquake-sequence frameworks, this concept is often extended to state-dependent fragility formulations, where the structural response to a subsequent event depends on the damage accumulated during previous seismic excitations.

Among the EDPs commonly adopted for fragility assessment, displacement-based quantities such as maximum interstory drift ratio [34], maximum inelastic displacement [35], and residual drift [36] are widely employed [34–36]. Their widespread use is mainly due to the fact that displacement-based response quantities are directly employed in seismic codes and performance-based assessment procedures to define both local and global structural capacities, allowing damage-state thresholds to be associated with physically interpretable displacement levels.

However, when seismic sequences are considered, peak displacement-based EDPs may present some limitations, since they are inherently non-cumulative and may not fully capture the progressive damage accumulation induced by repeated seismic loading. Previous studies have shown that this aspect may lead to statistical inconsistencies in fragility relationships and biased

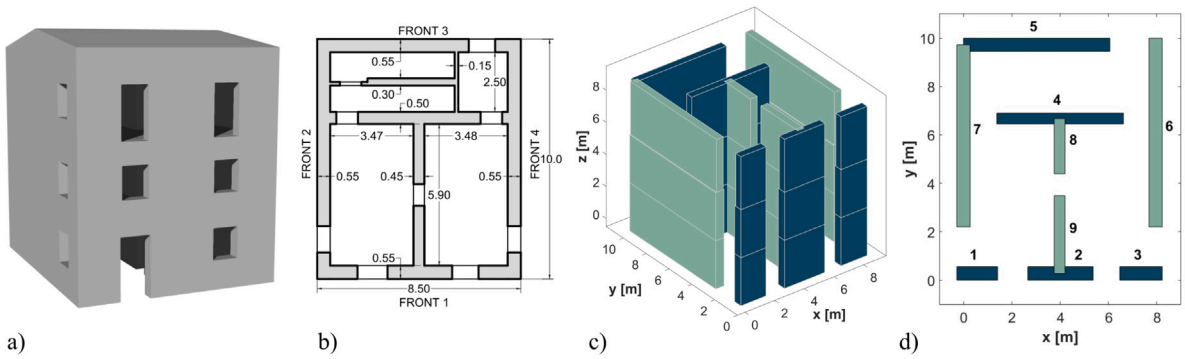

Fig. 1. Benchmark masonry structure: (a) 3D view; (b) plan; (c) E-PUSH 3D model; (d) E-PUSH plan.

estimates of post-MS vulnerability [30]. For this reason, increasing attention has recently been devoted to cumulative energy-based EDPs capable of explicitly accounting for cyclic degradation and cumulative inelastic demand [37,38]. For example, Gentile and Galasso [37] proposed a framework for the derivation of state-dependent fragility relationships for RC frame structures subjected to seismic sequences, where hysteretic energy dissipation is employed as the primary demand parameter. Their results demonstrated the capability of energy-based quantities to capture cumulative damage effects while reducing inconsistencies in the resulting probabilistic models. Similarly, [38] proposed an energy- and displacement-based damage index within a component-based framework for URM buildings, showing improved representation of cumulative damage accumulation during earthquake sequences.

Despite the aforementioned limitations, displacement-based EDPs remain widely adopted also in recent studies on seismic fragility and risk assessment under earthquake sequences [33]. In the present study, the adopted EDP for damage assessment is displacement-based and corresponds to the spectral displacement associated with the structural performance point obtained through the capacity spectrum method. Damage states are therefore defined through displacement thresholds, and exceedance probabilities are evaluated by comparing the computed displacement demand with the corresponding DS displacement capacities. The adoption of this EDP is consistent with the adopted capacity spectrum framework and enables a computationally efficient derivation of vector-valued MS–AS fragility surfaces.

2.3. Intensity measure selection

In fragility and vulnerability assessment, the choice of the IM plays a fundamental role in establishing the relationship between seismic input and structural response. An optimal IM should provide efficient, sufficient, and stable predictions of structural demand while minimizing record-to-record variability and dependence on additional ground-motion characteristics. Within earthquake-sequence frameworks, the selection of the IM becomes even more critical, since it directly affects the representation of coupled MS–AS events, the ground-motion selection and scaling procedures, and the resulting fragility formulation.

It is well established that PGA is not always the most appropriate IM for the derivation of fragility curves, as it does not fully capture the spectral characteristics of ground motions governing structural response. Several studies have shown that alternative IMs, such as the spectral acceleration at the fundamental period of vibration *Sa(T1)*, the average spectral acceleration over a range of relevant structural periods, *AvgSa*, or other advanced IMs accounting for ground-motion velocity and spectral shape effects, can significantly reduce record-to-record variability and improve the efficiency of fragility estimates and collapse assessment. For example, Dávalos and Miranda demonstrated that the filtered incremental velocity provides improved efficiency and sufficiency in collapse estimation compared to traditional IMs, by accounting for relevant time-domain characteristics of seismic records [39]. Similarly, O'Reilly showed that *AvgSa* may provide more stable and less biased response predictions than conventional IMs, such as *Sa(T1)*, for non-ductile infilled RC systems, where the response may be strongly influenced by spectral shape and velocity-related characteristics of the input motion [40].

It is also acknowledged that PGA cannot explicitly capture the increase in the natural period associated with stiffness degradation in masonry structures. In this regard, $AvgSa$ has been shown to better account for higher-mode effects and period elongation due to non-linear deformations [41]. Nevertheless, PGA presents several practical advantages. For example, it is one of the most employed IMs in post-earthquake damage surveys, because its records are less sensitive than the Peak Spectral Acceleration (PSA) to few operating seismic stations [42]. For this reason, several empirical fragility functions are based on PGA [43]. In addition, PGA is recommended in the Italian Building Code [44] for safety checks of mechanisms at low-level walls.

Moreover, several previous studies have successfully used PGA for ground motion selection and fragility derivation, within simplified non-linear static (pushover) frameworks, particularly for low-rise and relatively stiff URM buildings whose response is often governed by short-period behavior and high-frequency ground-motion components [45]. In this regard, recent studies have also shown that PGA may still provide satisfactory correlations with observed damage for masonry building classes [46]. Notable examples are [47], who used PGA to develop empirical fragility functions for masonry prototypes employing non-linear stochastic

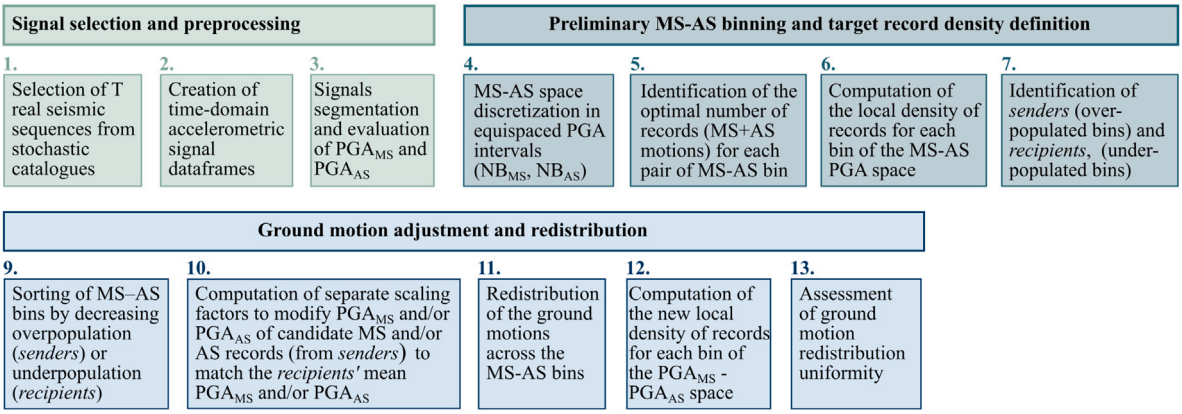

Fig. 2. Procedure for selecting and adjusting MS–AS ground motion sequences.

analyses, and [42], who derived fragility relationships for local failure mechanisms in URM buildings employing PGA as the adopted IM.

Therefore, while more advanced IMs may enhance the efficiency and sufficiency of fragility predictions, the use of PGA in this study represents a practical compromise between physical representativeness and methodological simplicity, considering both the adopted simplified framework and the interest in investigating the global behavior of low-rise and relatively stiff URM buildings, and the proposed methodology can be readily extended to other IMs in future applications. In addition, the adoption of PGA allows a straightforward definition of coupled MS–AS intensity pairs and simplifies the conditional balancing and scaling procedures employed for the construction of the bivariate fragility surfaces.

2.4. Ground motion selection

The selection of ground motion records is a key step in the derivation of fragility curves. Given an IM describing the seismic input, ground motions should be selected within a range of IM values that is capable of driving the structure to the target DS [48]. If the selected records are not properly chosen – being either too strong or too weak relative to the DS of interest – the resulting fragility curve may not be representative of the actual structural behavior.

This selection process becomes particularly complex when the behavior of structures under seismic sequences is investigated. From a mathematical perspective, the selection of ground motion records turns into a multi-dimensional optimization problem, as it involves simultaneously balancing multiple, often conflicting criteria or objectives, such as the correlation between MS and AS intensity measures, the spectral shape of each motion, and the timing between events, to name a few.

A simple procedure that can be employed to select and scale ground motions is illustrated in Fig. 2.

In this study, seismic sequences (horizontal components), characterized by a magnitude ranging from 5.01 to 9.08, are assumed to be composed of two signals, i.e., MS and AS. Three stochastic catalogs of seismic sequences have been used for this purpose: [49] for worldwide shallow crustal earthquakes (PEER-NGA database — 172 sequences), [50] for Japanese crustal/inslab/interface earthquakes (K-NET, KiK-net and SK-net databases — 531 sequences), and [51] for the 2016 Kumamoto, Japan, earthquake (K-NET and KiK-net - 28 sequences). The chosen catalogs resulted in a total T of 731 sequences, with a number of ground motions per sequence ranging from 2 to 26.

The adopted datasets include seismic sequences classified as MS–AS records within the reference catalogs. No additional seismological discrimination between strictly causal ASs and potentially triggered events was introduced in the present study, as the focus is placed on the structural response to sequential seismic events rather than on the physical mechanisms governing earthquake interaction.

For each sequence, a time-domain accelerometric signal dataframe is created from the raw data, consisting of acceleration values and sampling rate.

Each signal is then segmented according to the number of records. For those segments containing the MS and AS, the corresponding peak ground accelerations, PGA_{MS} and PGA_{AS}, are identified as the maximum absolute acceleration values.

Subsequently, the ground motion selection procedure involves defining a number of intervals that divide the mainshock and aftershock IM values – NB_{MS} and NB_{AS}, respectively – to achieve a reasonable discretization of the MS and AS PGA space. The resulting number of bins is $NB_{MS} \times NB_{AS}$, where each bin corresponds to a subregion of the joint MS–AS IM space, bounded by upper and lower PGA thresholds for both MS and AS events.

Fig. 3 shows the distribution of PGA of the MSs and ASs from the original catalog. The original ground motion sequences are not well distributed across the ranges of IM for both MS and AS. As expected, most of the sequences fall within the intervals delimited by the lowest values of MS and AS PGAs.

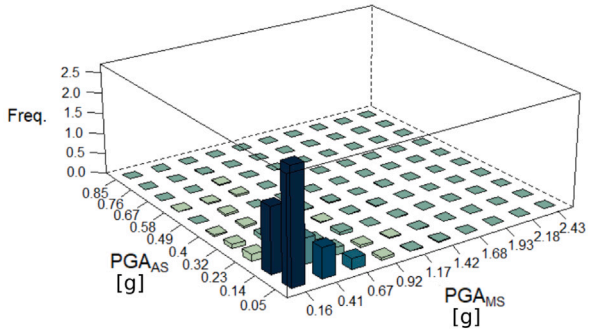

Fig. 3. Histogram of MS–AS pairs from the original ground motion record sets.

Therefore, ground motion records need to be manipulated to cover a broader range of IMs [52]. A very simple approach that allows seismic motions to be scaled, without losing the coherence between the MS and AS of the original dataset, is applied.

The optimal solution of the optimization problem $tr_{cond\,EQ}$ requires that each bin has a number of sequences equal to the total number of ground motions in the original catalog T, divided by the number of bins, $NB_{\mathrm{MS}} \times NB_{\mathrm{AS}}$. Therefore, the target number of records assigned to each bin of the MS–AS domain is computed as:

$$tr_{cond\,EQ} = \frac{T}{NB_{MS} \times NB_{AS}} \tag{1}$$

The local density of ground motions for each bin of the MS–AS space, N_{ij}, is evaluated as:

$$N_{ij} = \sum_{k=1}^{T} I_{ij}^{(k)} \tag{2}$$

where:

$$I_{ij}^{(k)} = \begin{cases} 1 & \text{if } PGA_{MS}^{(k)} \in [LB_{MS,i}, UB_{MS,i}] \\ & \text{and } PGA_{AS}^{(k)} \in [LB_{AS,j}, UB_{AS,j}] \\ 0 & \text{otherwise} \end{cases} \tag{3}$$

where LB and UB identify the lower and upper bounds, respectively, and the subscript specifies whether it refers to the MS or AS bins.

Bins satisfying:

$$N_{ij} > tr_{cond\,EQ} \tag{4}$$

are classified as *sender bins*, whereas bins with:

$$N_{ij} < tr_{cond\,EQ} \tag{5}$$

are *recipient bins*. Then, a procedure of conditional statistical balancing follows, aimed at homogenizing the distributions of MS and AS PGAs in their joint domain by optimizing the representativeness and reducing local frequency imbalances (i.e., overpopulated and underpopulated bins).

First, sender bins are sorted in descending order of ground motion overpopulation, and recipient bins in descending order of underpopulation — with the most overpopulated bins and the most in-need bins prioritized. For each sender bin, records are iteratively transferred toward recipient bins according to decreasing order of overpopulation and underpopulation. The target values adopted for scaling are the bin midpoints, $\overline{MS}$ and $\overline{AS}$ for the MS and AS bins, respectively:

$$\overline{MS} = \frac{LB_{MS} + UB_{MS}}{2} \tag{6}$$

$$\overline{AS} = \frac{LB_{AS} + UB_{AS}}{2} \tag{7}$$

where $LB_{MS}, UB_{MS}, LB_{AS}$ and UB_{AS} represent the lower and upper bounds of the MS and AS bins respectively.

Then, to reduce the unbalanced distribution among different bins, MS and AS ground motions are transferred from overpopulated bins to underpopulated bins by scaling the PGA_{MS} and/or PGA_{AS} of the senders so as to fall within the PGA of the recipient bin. In particular, the scaling factors applied were computed as:

$$SF_{MS} = \frac{\overline{MS}}{PGA_{MS}}; \quad SF_{AS} = \frac{\overline{AS}}{PGA_{AS}} \tag{8}$$

Scaling is only applied when a transferred sequence's IM falls outside the target recipient bin bounds.

Alternative optimization-based procedures for ground-motion selection and scaling could also be adopted, such as simulated annealing algorithms (e.g., [52]) or other metaheuristic optimization strategies (e.g., [53]) recently proposed in the literature for vector-valued seismic record selection problems. These approaches may provide a more optimal balancing of the target IM domain by minimizing predefined objective functions accounting for spectral compatibility, scaling penalties, or statistical representativeness. However, such methods generally require iterative optimization procedures, calibration of multiple control parameters, and increased computational effort.

In the present study, a simpler conditional balancing strategy was intentionally adopted in order to preserve the physical consistency of the original MS–AS sequences while maintaining a transparent and computationally efficient framework suitable for large-scale fragility analyses. The proposed approach does not aim at achieving a globally optimal distribution of the seismic sequences within the MS–AS intensity domain, but rather at obtaining a sufficiently uniform coverage while limiting excessive manipulation of the original records.

2.5. Software module

In this work, a tailored methodology for the non-linear static analysis of masonry buildings is proposed, utilizing the E-PUSH program developed by Croce et al. [54]. The methodology is summarized in Fig. 4. E-PUSH is open-source software specifically designed to simulate the seismic behavior of masonry structures through non-linear static (pushover) analyses. Its reliability has been validated through comparison with experimental results from laboratory-tested masonry prototypes [54], as well as through application to multiple real-world case studies – including the benchmark structure investigated in this work – by benchmarking its predictions against those obtained using commercial software [55].

The program adopts a macro-element approach based on the equivalent frame idealization, where shear-resistant walls are discretized into flexible piers connected at their ends via rigid links. The resistance of each element is assessed against various failure mechanisms, including diagonal shear and in-plane bending, in line with relevant design codes (i.e., [44]). The non-linear behavior of the walls subjected to constant vertical loads and cyclic horizontal loads is idealized by means of a bilinear envelope, characterized by an initial elastic slope k_y and a plastic plateau corresponding to the shear resistance of the wall and limited by the ultimate inter-story drift δ_u (see black curve in Fig. 4). The key assumptions adopted in this study are thus as follows:

- only walls extending from the foundations to an upper floor are considered shear-resistant elements;
- each shear wall contributes only with its in-plane stiffness, while out-of-plane stiffness is neglected;
- backbone curve, that is the force–deformation relationship of each wall, is approximated by a bi-linear curve bounded by the elastic drift d_e and an ultimate drift d_u, reflecting inter-story drift limits;
- at each step of the pushover analysis, the inter-story drift of each shear resistance wall, d, is checked against the elastic and ultimate drift (d_e and d_u). If $\delta < d_y$ the wall is still in its elastic phase with stiffness k_y. If $d_e < d \leq d_u$ the wall exhibits a plastic behavior, and its apparent stiffness k'_y is computed as $(d_e k_e)/d$. Finally, if $d > d_u$ the wall is considered collapsed, losing both lateral stiffness and shear resistance, and is assumed to support only vertical loads.
- the analysis ends either when the base shear drops below a defined percentage, 80%, of the maximum base shear resistance, or the wall belonging to the same floor collapses. In this way, the global capacity curve (CC) of the structure e.g., the global base shear–displacement response of the entire building can be obtained;
- after the pushover analysis, the whole structure is transformed into an equivalent SDOF system, allowing performance evaluation through the N2 method [56] or the Capacity Spectrum Method [57] on the ADRS (Acceleration-Displacement Response Spectrum) plane domain.

Leveraging its low computational effort, sensitivity analysis and uncertainty propagation have been integrated into the E-PUSH program to provide a probabilistic assessment of the seismic performance of masonry buildings, considering the relevant uncertainties related to masonry material parameters and in-plane displacement capacity [54]. However, in the present study, all mechanical properties have been treated deterministically, as summarized in Table 1 to isolate the effect of ground motion variability and sequence-dependent damage accumulation on the derived fragility surfaces, avoiding additional sources of dispersion related to material uncertainty.

The original software is distributed "open source" under a Creative Commons License (CC BY-ND 4.0). The EPUSH software [58] has been recently updated developing a web-based API and new functionalities to extract structural data directly from Building Information Models. The updated version is now available on GitHub and Zenodo [59].

2.6. Vector-valued fragility and vulnerability surfaces conditioned on MS and AS intensity levels

The approach presented in this study aims to realistically simulate the impact of actual MS–AS sequences without assuming that the structure reaches a predefined DS due to the MS. Instead, the method accounts for the damage directly caused by the MS event. In this framework, fragility relationships are formulated as bivariate surfaces conditioned on both MS and AS intensity levels. Therefore, the proposed methodology differs from traditional state-dependent fragility approaches (e.g., [1,12,20]), in which fragility is conditioned on the structural DS attained after the MS, as well as from ground-motion-dependent formulations explicitly accounting for record-specific characteristics beyond the adopted IM values, such as spectral shape, velocity-related parameters, or duration effects (e.g., [39,40]). The proposed approach is instead based on a vector-valued IM representation of sequential seismic

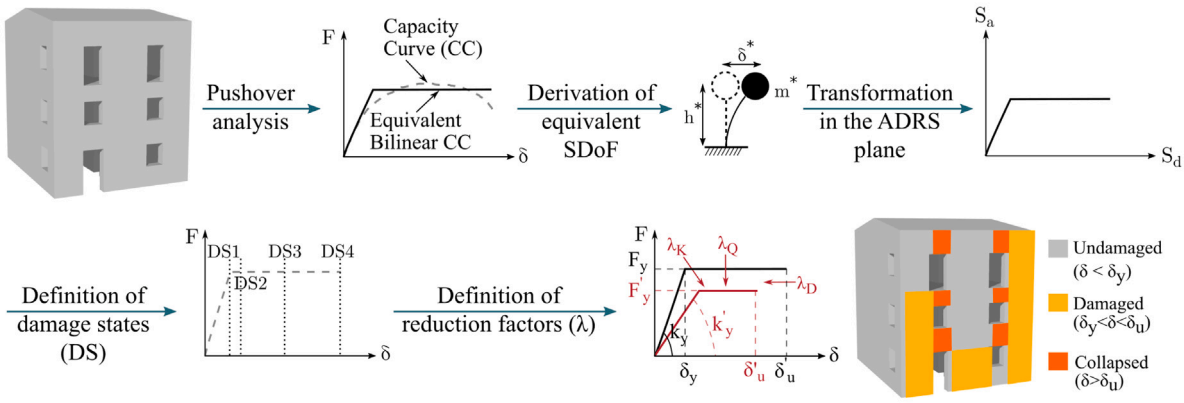

Fig. 4. Definition of DSs starting from the pushover of the undamaged benchmark building.

events, where the structural response is associated with coupled MS–AS intensity levels. This choice was motivated by the intention to directly describe the structural response within the joint MS–AS intensity domain without introducing intermediate damage-state classifications between seismic events. In this way, the proposed approach allows a continuous representation of damage accumulation induced by sequential earthquakes while preserving a relatively simple and computationally efficient framework for the construction of bivariate fragility surfaces. This aspect is particularly relevant for masonry structures, whose seismic response is strongly influenced by progressive stiffness degradation and cumulative damage effects. In this sense, the approach described in this study differs from more traditional state-dependent fragility approaches, which condition the structural response to the AS on the DS attained after the MS, thereby reducing uncertainties associated with the mapping between the first-event IM and the resulting structural condition.

The proposed procedure consists of the following steps:

- Conduct a non-linear static analysis of the undamaged structure to obtain its global capacity curve;
- Determine the performance point for the MS spectrum, as detailed in Section 2.6.2;
- Update the structural model to reflect the damage level reached by the structural elements at the performance point, incorporating appropriate reduction factors;
- Perform a non-linear static analysis of the damaged structure to derive the updated global capacity curve of the building;
- Identify the performance point for the updated global capacity curve using the AS spectrum;
- Repeat steps 1 through 5 for each ground motion sequence considered (in this case, two: the MS and AS events);
- Derive fragility surfaces to quantify the probability of exceeding different DSs as a function of MS and AS intensity measures, following the procedure in Section 2.6.4.

2.6.1. Non-linear static analysis for the undamaged structure

First, a pushover analysis is carried out to derive the global capacity curve of the undamaged benchmark building and define the relevant DS. To enable the evaluation of structural response under seismic sequences, a new functionality for performing sequential pushover analyses has been implemented in the E-PUSH software. The procedure for defining the DSs – illustrated in Fig. 4 – includes the following steps:

- A non-linear static analysis is conducted on the undamaged structure to derive the global capacity curve of the building. The resulting force–displacement curve of the MDOF is then transformed into that of an equivalent SDOF. An idealized bi-linear elasto-plastic curve is subsequently fitted in the acceleration displacement plane [60]. The derived capacity spectrum is characterized by an equivalent yielding displacement $S_{d,y}$, a maximum acceleration $S_{a,y}$ and an ultimate displacement $S_{d,u}$.
- With reference to the global capacity curve, four DSs representative of increasing levels of structural damage are defined consistently with the macroseismic interpretation proposed for masonry structures by [45]. In particular, DS1 corresponds to slight damage associated with the onset of distributed cracking and limited stiffness degradation; DS2 represents moderate damage characterized by significant cracking and reduction of structural stiffness; DS3 corresponds to severe damage involving extensive cracking and substantial degradation of the lateral-load-resisting system; finally, DS4 represents near-collapse conditions associated with the attainment of the ultimate structural capacity. The occurrence of these DSs is numerically identified through displacement thresholds defined along the global capacity curve according to [45]: DS1 (slight damage) corresponds to the displacement at $0.7 \cdot S_{d,y}$, DS2 (moderate damage) to that at $1.5 \cdot S_{d,y}$, DS3 (severe damage) to that at $0.5 \cdot (S_{d,y} + S_{d,u})$, and DS4 (near collapse) to the attainment of the ultimate displacement $S_{d,u}$.

Each point along the global capacity curve represents a distinct structural configuration, where individual structural elements, specifically, masonry walls, can be in the elastic phase, plastic phase, or fully collapsed. When a masonry wall enters the plastic phase

Table 2
Modeling criteria for damaged walls for a URM2B structure (weaker pier component, with bed joint sliding behavior mode) from FEMA 306 [61].

Damage level	λ_K	λ_Q	λ_D
Insignificant	0.9	0.9	1
Moderate	0.8	0.6	1
Heavy	0.6	0.6	0.9

($\delta > \delta_y$), its stiffness decreases. The reduced stiffness k'_y is defined as the ratio between the shear resistance V_y and the displacement. A stiffness reduction factor (λ_K) is then calculated as the ratio between k'_y and the initial (elastic) stiffness of the element k_y. According to FEMA 306 [61], three damage levels, namely *insignificant, moderate, heavy*, are associated with the observed damage condition of the component, and corresponding modification factors for stiffness (λ_K), strength (λ_Q), and ductility (λ_D) are then provided for each level. In the present analytical framework, however, no direct observational damage classification is available at the wall level. Therefore, the computed stiffness reduction factor λ_K is used as a numerical proxy to map each damaged wall to one of the FEMA 306 levels. This represents an additional modeling assumption adopted to translate the element-level degradation obtained from the pushover analysis into the FEMA 306 reduction-factor framework. Once the damage level is assigned, the corresponding λ_Q and λ_D factors are selected from the FEMA 306 recommendations for the URM typology and applied to update the wall strength and deformation capacity before the subsequent pushover analysis. The three FEMA-based damage levels are used to define capacity reduction factors at the element level, which in turn influence the global response and the attainment of the four displacement-based DSs defined above.

The reduction factors adopted in this study are taken from the FEMA 306 recommendations for URM wall systems and are mechanism-dependent. Therefore, they may vary for different masonry typologies or collapse mechanisms, such as flexural rocking, diagonal cracking, or shear sliding. The values adopted herein should not be interpreted as universally applicable, but rather as representative parameters suitable for the considered building class and modeling assumptions. In particular, the reduction factor values here adopted (Table 2) correspond to the URM2B structural typology, characterized by weaker pier components and bed-joint sliding failure mechanisms. Such factors were selected because the adopted case-study building exhibits mechanical and typological characteristics consistent with traditional URM buildings commonly found in Mediterranean and Central European regions, where in-plane shear damage and stiffness degradation are among the dominant seismic response mechanisms. Although no analogous factors are prescribed in European codes, the adopted parameters align with those used in [62] to model the strength degradation of masonry piers in the non-linear analyses of typical existing masonry buildings across European countries. The adopted parameters therefore provide a simplified yet physically consistent representation of the progressive degradation of masonry walls under sequential seismic loading.

It should be emphasized that the adopted procedure does not explicitly model the full hysteretic cyclic response and cumulative energy dissipation mechanisms associated with earthquake sequences, as would be achieved through non-linear time–history analyses. Rather, the proposed approach introduces a simplified representation of damage accumulation effects through phenomenological reduction factors accounting for progressive stiffness, strength, and ductility degradation at the wall level.

2.6.2. Evaluation of the performance points for the MS and AS spectra

Ground motions are selected according to the procedure described in Section 2.3 and their real spectra in the ADRS plane are compared with the computed capacity spectrum of the building according to the Capacity Spectrum Method (CSM) modified by [21] to be applied to real demand spectra. The method consists of discretizing the capacity spectrum from the yielding point in small displacement intervals Δ_i. An equivalent SDOF system is then associated to each Δ_i characterized by effective period, $T_{eff,i}$, equivalent viscous damping, ξ_i, and spectral reduction factor η_i:

$$T_{eff,i} = \sqrt{\frac{\mu_i}{1 + r(\mu_i - 1)}} T_{el} \tag{9}$$

$$\xi_i = 0.05 + C_{evd}\left(\frac{\mu_i - 1}{\pi \mu_i}\right) \tag{10}$$

$$\eta_i = \sqrt{\frac{0.07}{0.02 + \xi_i}} \tag{11}$$

where T_{el} is the elastic period corresponding to the elastic branch of the capacity spectrum, r is the hardening ratio assumed here equal to 0, and C_{evd} is equal to 0.67, considering elasto-plastic hysteretic behavior.

As shown in Fig. 5, when evaluating the performance point for the MS spectrum, different scenarios can occur:

- The global capacity curve (undamaged structure) intersects the elastic MS spectrum in the elastic branch, then damage does not occur, and the MS spectrum does not need to be scaled. The performance point is directly given by the intersection point.
- The global capacity curve (undamaged structure) does not intersect the elastic MS spectrum in the elastic branch, then damage occurs, and the MS spectrum needs to be scaled through η_i. Two possibilities arise from the comparison of the two spectra:

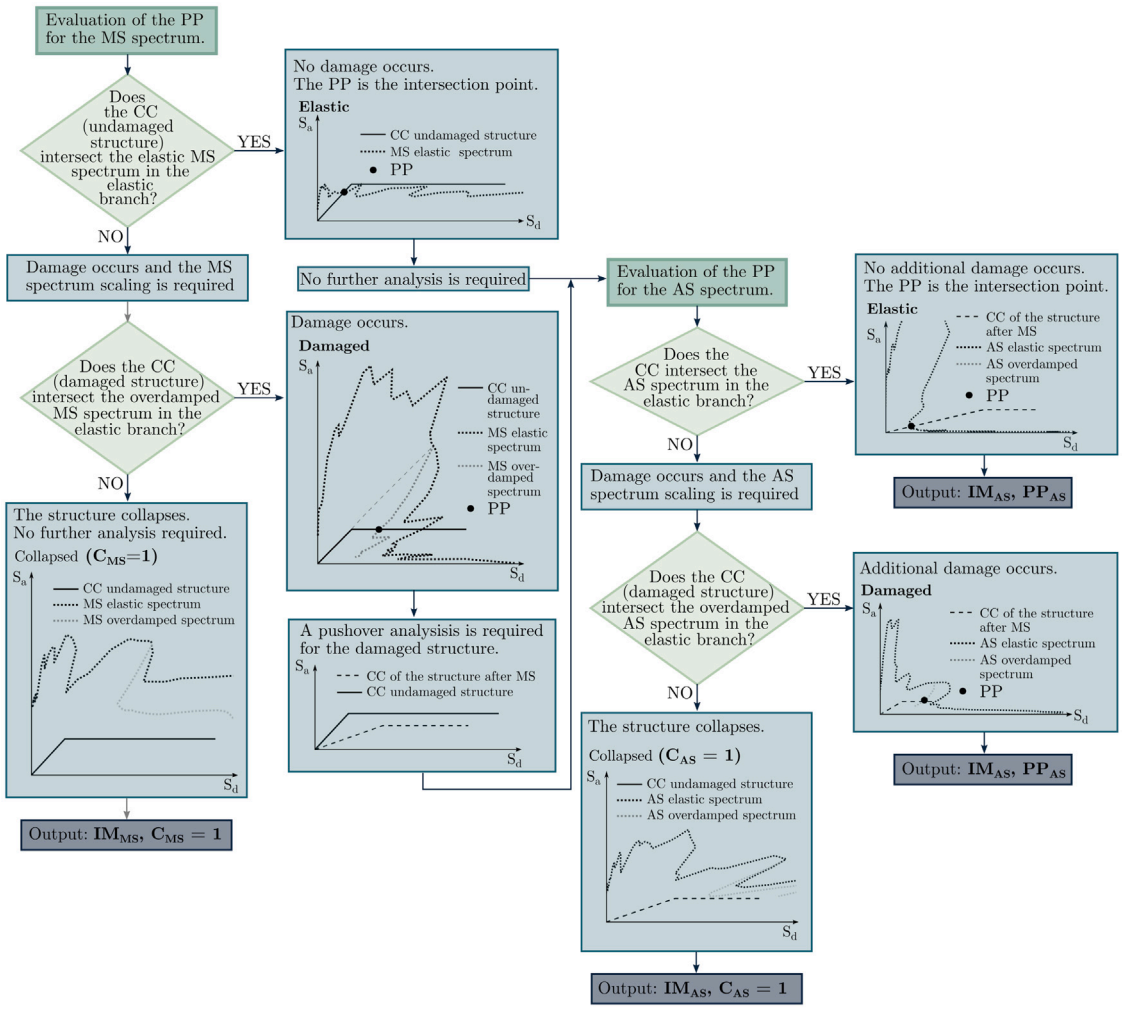

Fig. 5. Flowchart of the proposed procedure for deriving vector-valued MS–AS fragility surfaces.

- The global capacity curve does not intersect the overdamped MS spectrum, then the structure gets to the collapse (C) and no further analysis is required. As an output $IM_{\mathrm{MS}}, C_{\mathrm{MS}} = 1$, corresponding to a collapse probability equal to 100% (i.e., a deterministic collapse condition under the considered ground motion intensity level).
- The global capacity curve intersects the overdamped MS spectrum in the plastic branch. Another pushover analysis on the structure damaged according to the reached DS and reduction coefficients needs to be performed. The new global capacity curve (damaged structure) of the MDOF needs to be transformed into that of an equivalent SDOF, and an idealized bi-linear elasto-plastic curve is then fitted in the acceleration displacement plane [60].

Successively, the following step for deriving vector-valued fragility surfaces (conditioned on MS and AS intensity levels) that corresponds to the third step illustrated in Fig. 5 entails the evaluation of the performance point for the AS spectrum. As for the MS spectrum, different outcomes are contemplated:

- The global capacity curve (damaged structure) intersects the elastic AS spectrum in the elastic branch, then (additional) damage does not occur, and the AS spectrum does not need to be scaled. The performance point is directly given by the intersection point.
- The global capacity curve (damaged structure) does not intersect the elastic AS spectrum in the elastic branch, then (additional) damage occurs, and the AS spectrum needs to be scaled. Two possibilities arise from that:
  - The global capacity curve does not intersect the overdamped AS spectrum, then the structure collapses. As an output, the global capacity curve IM_{AS}, and $C_{\mathrm{AS}} = 1$.
  - The global capacity curve intersects the overdamped AS spectrum in the plastic branch. As an output $IM_{\mathrm{AS}}, PP_{\mathrm{AS}}$ are found.

2.6.3. Bivariate fragility functions

To develop the vector-valued fragility conditioned on MS and AS intensity levels surfaces, bivariate models are fitted to the results of the CSM analysis. The assumption of Multivariate Normality is first verified by means of the Mardia's test [63], and then a bivariate normal distribution is fitted to the sequences of ground motions (IM_{MS}, IM_{AS}) leading to a performance point exceeding the considered DS for the "*no collapse*" cases ($C_{\mathrm{AS}} = 0$). The corresponding probability density function is given by:

$$f_{DS}(IM_{MS}, IM_{AS}|C_{AS}=0) = \frac{1}{2\pi\sigma_{IM_{MS}}\sigma_{IM_{AS}}\sqrt{1-\rho^2}} \exp\left(-\frac{1}{2(1-\rho^2)}\left[\left(\frac{IM_{MS}-\mu_{IM_{MS}}}{\sigma_{IM_{MS}}}\right)^2 - 2\rho\left(\frac{IM_{MS}-\mu_{IM_{MS}}}{\sigma_{IM_{MS}}}\right)\left(\frac{IM_{AS}-\mu_{IM_{AS}}}{\sigma_{IM_{AS}}}\right) + \left(\frac{IM_{AS}-\mu_{IM_{AS}}}{\sigma_{IM_{AS}}}\right)^2\right]\right) \tag{12}$$

where ρ is the correlation coefficient equal to:

$$\rho = \frac{\sigma_{IM_{MS}IM_{AS}}}{\sigma_{IM_{MS}}\sigma_{IM_{AS}}} \tag{13}$$

and $\sigma_{IM_{MS}IM_{AS}}$ is the covariance of IM_{MS} and IM_{AS}.

The same probabilistic model is adopted for the "*collapse*" cases ($C_{\mathrm{AS}} = 1$) induced by the sequence of MS and AS, i.e., $f(IM_{MS}, IM_{AS}|C_{AS}=1)$.

2.6.4. Fragility surfaces

The vector-valued fragility surfaces conditioned on MS and AS intensity levels, that is the probability of exceeding a specific DS threshold due to the AS ground motion (IM_{AS}) given the performance point reached due to the MS (IM_{MS}), is obtained as follows:

$$P(DS_{\mathrm{MS+AS}}|IM_{\mathrm{MS}}, IM_{\mathrm{AS}}) = P(DS_{\mathrm{MS+AS}}|IM_{\mathrm{MS}}, IM_{\mathrm{AS}}, \text{"no collapse"})(1-[P(C|IM_{\mathrm{MS}}, IM_{\mathrm{AS}})(1-P(C|IM_{\mathrm{MS}})) + P(C|IM_{\mathrm{MS}})]) + P(C|IM_{\mathrm{MS}}, IM_{\mathrm{AS}})(1-P(C|IM_{\mathrm{MS}})) + P(C|IM_{\mathrm{MS}}) \tag{14}$$

combining the following terms:

- the probability of exceeding the DS threshold given that collapse does not occur, namely $P(DS_{\mathrm{MS+AS}}|IM_{\mathrm{MS}}, IM_{\mathrm{AS}}$, "*no collapse*"), which is obtained by fitting a multi-variate (i.e., bivariate) normal distribution to the sequence of ground motions leading to a performance point exceeding the considered DS;
- the probability of collapse, namely $P(C|IM_{\mathrm{MS}}, IM_{\mathrm{AS}})$, which is obtained by fitting a multi-variate (i.e., bivariate) normal distribution to the sequence of ground motions leading to the collapse of the structure;
- the probability of collapse given the MS, namely $P(C|IM_{\mathrm{MS}})$, which is obtained by fitting a normal distribution to the MS ground motions leading to the collapse of the structure.

2.7. Vulnerability surfaces

The mean damage ratio (MDR) represents the estimated cost to repair a building, expressed as a fraction of its total loss. MDR falls on a scale between 0 (no damage) and 1 (total loss/destruction). Here, this ratio is expressed as a function of the MS and AS intensity measures, and of the associated DS reached, and is calculated by combining fragility probabilities with damage-to-loss ratios, following Eq. (15):

$$MDR(IM_{\mathrm{MS}}, IM_{\mathrm{AS}}) = \sum_{k=1}^{3} P(DS_{\mathrm{k,MS+AS}}|IM_{\mathrm{MS}}, IM_{\mathrm{AS}}) \cdot c_k \tag{15}$$

where c_k is the cost of the repair/reconstruction factor associated with the (k)th DS, assumed here equal to 0.02, 0.3 and 0.68 for k = 1, 2 and 3, i.e. slight, moderate, and severe damage, respectively. c_k represents the percentage cost relative to the unit replacement cost (Euro/m^2) of residential buildings. These factors c_k are based on those proposed in [64], here adapted to four DSs. The fourth damage state, DS4, corresponding to near-collapse conditions is not included among the DSs considered in Eq. (15), as it directly corresponds to the total loss, e.g., to a MDR equal to 1. This approach is consistent with established loss-modeling methodologies, e.g., [65], in which fragility surfaces are mapped to economic loss via bin-integrated cost functions. In the present paper, Eq. (15) is evaluated over an (IM_{MS}, IM_{AS}) grid and visualized as a three-dimensional vulnerability surface. This surface can be subsequently employed into risk calculations for masonry buildings under earthquake sequences.

3. Results and discussion

3.1. Ground-motion selection

The application of the proposed scaling algorithm for the ground motion selection yields a set of ground motion sequences that preserves the inherent MS–AS consistency of the original catalog while providing a more uniform coverage of the target IM space. Fig. 6 shows the distribution of scaled MS–AS pairs, resulting from the adoption of scaling factors ranging approximately between 0.001 and 14 for MS records and between 0.03 and 52 for AS records. However, the distribution of scaling is highly non-uniform, with the majority of records undergoing moderate adjustments (mean scaling factors of approximately 1.69 and 2.69, and coefficients of variations of around 0.85 and 2.16 for MS and AS, respectively), while only a limited subset required significantly larger modifications. These larger scaling factors are mainly associated with AS records (~10% of AS records) and arise from the intrinsic characteristics of the adopted seismic catalogs, where ASs are generally much weaker than the corresponding MSs. Consequently, populating regions of the MS–AS domain characterized by comparable MS and AS intensity levels requires stronger scaling of the AS records. Although such scaling may distort the original spectral content in extreme cases, the proposed procedure prioritizes preservation of MS–AS pairing and physical sequencing while ensuring sufficient coverage of the joint intensity domain.

The scaled dataset adequately populates the border surface of the MS-PGA-AS-PGA space, as intended. However, some bins remain less populated than others, particularly those representing combinations characterized by AS intensities comparable to or larger than the corresponding MS intensity levels. This may reduce the statistical robustness of the fitted fragility surfaces in these regions, owing to the limited number of available seismic sequences supporting the probabilistic estimation. This is a direct consequence of retaining the physical coupling between the original MSs and ASs, which inherently limits the admissible scaling range. The resulting imbalance reflects the intrinsic characteristics of the adopted ground-motion catalog and the physical unlikelihood of strong ASs relative to the corresponding MSs. Further scaling would require excessive distortion of the records and is therefore avoided. Consequently, the adopted methodology reflects a deliberate compromise between spectral realism and statistical representativeness of the MS–AS space. Future developments could investigate advanced record-selection or synthetic-sequence generation procedures to improve the statistical representativeness of sparsely populated regions of the MS–AS space.

It should be emphasized that the adopted scaling strategy was not intended to generate site-specific or spectrally optimized ground-motion suites, but rather to enable an exploratory and sufficiently uniform sampling of the joint MS–AS intensity domain required for the construction of vector-valued fragility surfaces. In this sense, relatively large scaling factors were intentionally tolerated in sparsely populated regions of the MS–AS space, particularly for sequences characterized by AS intensities comparable to or larger than the corresponding MS intensities. Although such scaling may reduce the physical realism of individual records in extreme cases, the adopted procedure prioritizes preserving the original temporal and physical consistency of the seismic sequences while enabling investigation of cumulative damage effects over a broad range of coupled intensity scenarios. The proposed framework should therefore be interpreted primarily as a proof-of-concept methodology aimed at exploring sequence-dependent fragility trends and damage accumulation mechanisms, rather than as an optimized record-selection strategy for site-specific structural assessment.

However, alternative scaling factors could have been considered. For instance, one could minimize a distortion metric, such as the one defined in Eq. (16), which accounts for the interplay between MS and AS intensities, with the MS and AS scaling factors SF_{MS} and SF_{AS} computed according to Eq. (8).

$$SF = \sqrt{SF_{MS}^2 + SF_{AS}^2} \tag{16}$$

Methods based on minimizing the Euclidean norm of the scaling factors are often preferred when dealing with vector-valued IMs, as they help balance the relative contributions of multiple IMs and achieve a more coherent scaling. However, this combined-scaling approach was not pursued here. Given that the primary objective was to obtain a more uniform coverage of the domain shown in Figs. 3 and 6, the selected algorithm prioritizes coverage uniformity over perfect balancing of the individual scaling factors. This is confirmed by comparing the histograms in Figs. 3 and 6, which clearly show an improved uniformity of the scaled MS–AS distribution, with PGA_{MS} and PGA_{AS} varying between 0.03 g and 0.49 g, and 0.01 g and 0.23 g, respectively.

Adopting alternative IMs, such as *Sa(T1)* or *AvgSa*, could influence both the ground motion selection process and the resulting fragility estimates, particularly for masonry structures exhibiting significant stiffness degradation and period elongation during damage progression. In such cases, IMs accounting for spectral shape and velocity-related characteristics of ground motions may reduce record-to-record variability and improve the consistency of the estimated structural response under seismic sequences.

In addition, the use of alternative IMs would also affect the scaling and balancing strategy adopted herein, since the distribution of seismic sequences within the MS–AS intensity domain would depend on spectral rather than purely amplitude-based characteristics. A comprehensive comparison between different scalar or vector-valued IMs would require the reformulation of the record selection, scaling, and fragility derivation procedures within the adopted MS–AS framework and is therefore beyond the scope of the present study. However, the proposed methodology is general and can be extended to alternative IM definitions.

3.2. Cloud-CSM fragility analysis

Having established a suitably distributed set of MS and AS intensity pairs, then the resulting bivariate vector-valued fragility surfaces conditioned on MS and AS intensity levels obtained from the scaled dataset were derived following the procedure reported in Section 2.6.

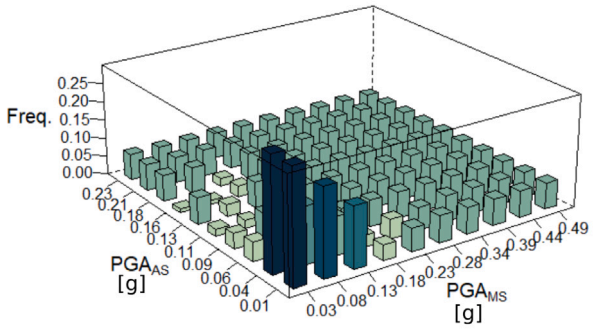

Fig. 6. Histogram of MS–AS pairs from the adjusted ground motion record sets.

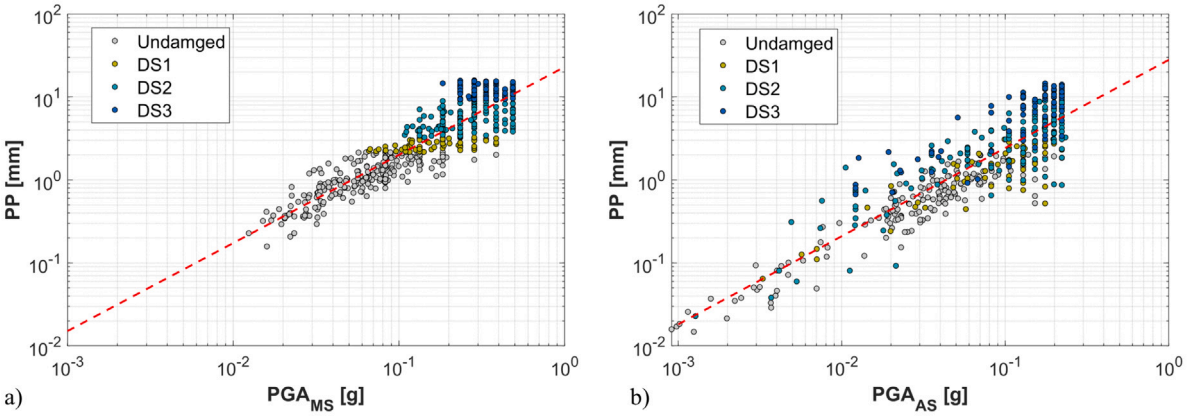

Fig. 7. Relationship between the IM and the performance points obtained using the cloud-CSM for the undamaged structure: (a) MS only; (b) After the MS–AS sequence.

Fig. 7 presents the results of the cloud analysis for the undamaged structure under (a) MS-only excitation and (b) sequential MS–AS excitation. The horizontal axis reports the PGA of the MS and AS, while the vertical axis depicts the corresponding displacement at the performance point (PP) of the structure.

As shown in Fig. 7(a), under MS-only scenarios, the response is well-correlated with PGA_{MS} for low-to-moderate intensity levels, as confirmed by the linear fitting (dashed red line) in the logarithmic plane. However, as damage begins to accumulate at higher intensities, a clear increase in scatter is observed, and data points corresponding to DS2 and DS3 branch off.

Fig. 7(b), in contrast, illustrates the sequential response of the structure under AS shaking. Even for ASs of relatively modest intensity, the performance point displacements are significantly larger than those from the MS-only case due to the prior DS of the structure. This reflects the increased vulnerability of the structure after the first event — the AS is superimposed on an already weakened system, producing larger displacements even under comparatively low AS-PGA levels. The data for DS2 and DS3 become more widespread and shifted upward relative to the red dashed mean-trend line. Overall, this comparison highlights the substantial role of damage accumulation and residual capacity on the seismic response of masonry structures subjected to ground motion sequences. The scatter of points in Fig. 7(b) is considerably greater than in Fig. 7(a), and most data for damaged states lie well above the mean trend defined by the red dashed fit. This further supports the need to explicitly account for the sequence of ground motions, pinpointing the MS–AS PGA values with the bivariate formulation.

3.3. Validation against non linear time history analyses

As a consistency check within the assumptions of the adopted simplified framework, additional NLTHAs were performed on an equivalent SDOF representation of the benchmark building. The objective of this comparison is to verify whether the proposed sequential capacity-spectrum procedure produces displacement demands broadly consistent with those obtained from a dynamic analysis based on the same SDOF idealization. The NLTHAs were developed following the SDOF idealization for low-rise masonry buildings proposed in [66], in which the global capacity curve obtained from pushover analysis is converted into an equivalent bilinear backbone defined by the yielding point (u_y, F_y), the ultimate displacement u_c. To represent cyclic degradation and energy dissipation in a consistent manner with experimental evidence on masonry structures, the damping was modeled through an

Table 3
Ratio of fragility parameters, median μ and dispersion β, obtained from the proposed method and NLTHAs for the MS ground motion and the sequence MS–AS.

State	MS		AS	
	μ	β	μ	β
Undamaged	0.95	0.99	1.10	0.98
DS1	0.89	1.05	0.80	1.22
DS2	1.02	0.98	1.15	0.86
DS3	1.09	0.87	0.98	0.95

equivalent damping ratio that evolves with ductility demand. The hysteretic damping law was anchored to the values provided in [67] for the same elastic period of the equivalent SDOF of the investigated structure, T_0=0.179s, $\xi_{hyst} = 0.153$ and $\xi_{vd} = 0.026$, and at each integration step the instantaneous ductility was used to update the damping coefficient, ensuring that the dissipated energy per cycle matched the target hysteretic behavior. The maximum displacements recorded in the analyses for the ground motion sequences are then compared to the performance points derived according to the proposed method. As a measure of accuracy, ratios of fragility parameters [68], median μ and dispersion β, are evaluated for each DS. The resulting ratios, reported in Table 3, demonstrate an overall agreement with values falling within ±20%, and should therefore be interpreted as evidence of internal consistency between the proposed sequential pushover-based procedure and the adopted SDOF-NLTHA benchmark. A further confirmation of the consistency of the results is derived from the comparison of the fragility surfaces obtained with the two methods, which are shown as two-dimensional contour plot projections in Fig. 8. The shape and overall trends of the fragility surfaces are highly similar, with the proposed approach generally yielding slightly more conservative probability estimates. Because both analyses rely on the same equivalent SDOF idealization derived from the pushover capacity curve, the comparison does not demonstrate the accuracy of the methodology relative to detailed non-linear MDOF simulations or experimental observations. Such broader validation is left for future work.

3.4. Vector-valued fragility and vulnerability surfaces conditioned on MS and AS intensity levels

Following the procedure described in Section 2.6.3, multivariate normality was first assessed for the different DSs using Mardia's test. The resulting *p*-values for skewness (0.07, 0.12, 0.13, and 0.018) and kurtosis (0.83, 0.93, 0.87, and 0.88) are above the 0.05 significance level in most cases, except for a marginal deviation in skewness for the collapse case. Overall, these results support the adequacy of the bivariate normal approximation for DS1–DS3, while indicating a limited departure from multivariate normality for the collapse cases. The Q–Q plots of the squared Mahalanobis distances provide an additional graphical check of this assumption. They show minor deviations from the theoretical χ^2 line, particularly in the upper tail, but these discrepancies are not systematic and remain within the range typically observed for typical sample sizes encountered in fragility analysis. Moreover, the confidence ellipses constructed from the empirical covariance matrix align well with the data cloud for all three DSs, consistently reproducing the elliptical contours expected under a bivariate normal distribution [69]. Overall, the combined evidence supports the use of a bivariate normal model for the fitted fragility surfaces, while acknowledging the limited deviation observed for the collapse case.

Based on these results, bivariate functions are fitted and the vector-valued fragility surfaces conditioned on MS and AS intensity levels (PGA_{MS} and PGA_{AS}) are derived for each damage state (DS1, DS2, DS3) and collapse. These fragilities are shown as two-dimensional contour plot projections in Fig. 8 and as surfaces in Fig. 9a.

Each fragility surface illustrates the conditional damage probability as a smooth, increasing function over the two-dimensional IM space. Generally, as expected, all surfaces exhibit a monotonic increase in the probability of reaching or exceeding each DS as both PGA_{MS} and PGA_{AS} increase. More specifically:

- DS1 (yellow) is reached at comparatively low levels of ground motion intensity, especially driven by the MS, with a less pronounced sensitivity to the AS intensity once the MS intensity is high.
- DS2 and DS3 (light and dark blue) require larger intensities of both MS and AS to occur with a certain probability, demonstrating the progressive damage accumulation.
- Collapse (red) occurs at high intensities of both MS and AS, representing the most severe end of the damage spectrum.

Notably, the surfaces are steepest along the PGA_{MS} axis and more gradual along the PGA_{AS} axis. This indicates that the MS is the primary driver of damage, while the AS plays a more secondary, cumulative role. These surfaces make it clear that structures already damaged by a strong MS are more vulnerable to even a moderate AS. For example, the probability of achieving DS3 with a MS characterized by a $PGA_{MS} = 0.15$ g that is about 1.5% can increase up to 11% with an AS characterized by the same PGA, or $P(DS3|PGA_{MS} = 0.3\text{ g}) = 37.3\%$ increase up to 70% and 91% for PGA_{AS}= 0.18 g and 0.21 g respectively.

These results support the need for immediate post-event inspections and targeted retrofitting for structures that have sustained substantial damage (e.g., reaching DS2–DS3), especially if ASs are expected, as often occurs. In addition, these surfaces can guide decisions on occupancy and access control after a strong MS. For example, if the structure experienced ground motions close to the DS2 threshold, emergency managers might restrict use until after AS risk decreases or repair is carried out.

Such a tool would be especially useful when the proposed two-event framework is applied to building prototypes (portfolios) instead of on a single construction as in the present case. In this case, the method would enable taking full advantage of not requiring

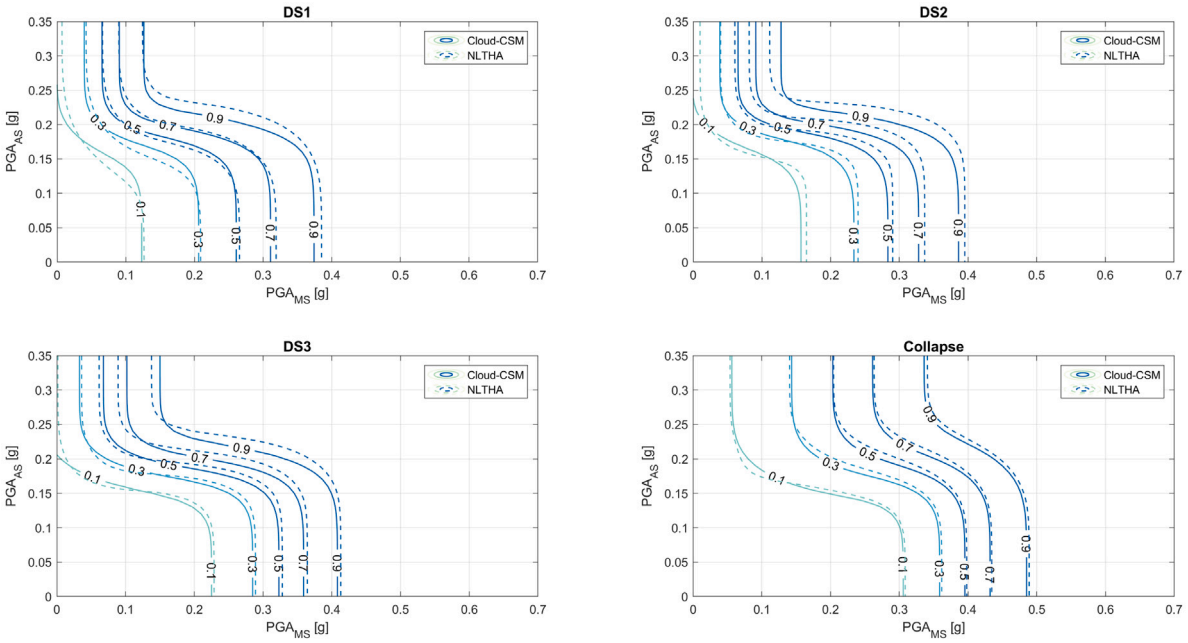

Fig. 8. Fragility surface contours for DS1, DS2, DS3 and collapse given PGA_{MS} and PGA_{AS}: comparison of the results obtained with the proposed approach (solid lines) and NLTHAs (dashed lines).

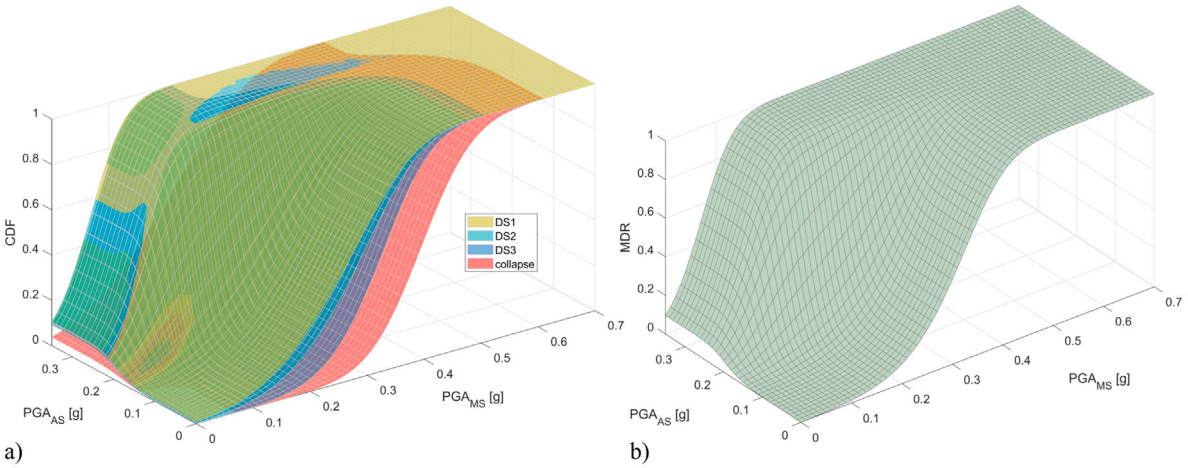

Fig. 9. (a) Fragility surfaces for DS1, DS2, DS3 and collapse given PGA_{MS} and PGA_{AS}; (b) Bivariate distribution function (CDF) of the MDR given PGA_{MS} and PGA_{AS}.

hypothesizing the DS reached due to the MS, as usually assumed to derive state-dependent fragility curves [12,20,30,52]. Therefore, a more comprehensive overview/understanding could be reached independent of the DS reached in the MS. The considerations would be rather related only to the PGA_{MS}.

Engineers could draw on the vector-valued fragility surfaces conditioned on MS and AS intensity levels obtained to appreciate the compound hazard posed by MS–AS sequences, which may lead to design strategies that explicitly account for capacity degradation or residual strength after a first event. Moreover, such fragility surfaces improve catastrophe models, many of which rely on a single IM to represent seismic events (e.g., peak ground acceleration or spectral acceleration at a given period) [70].

To complement the interpretation of the fragility surfaces discussed above, an additional consistency check was performed to assess their relative ordering. In a fully consistent fragility model, for a given pair of intensity measures, the probability of exceeding a higher damage state should not be larger than the probability of exceeding a lower damage state. Fig. 10 compares the contour lines corresponding to exceedance probability levels equal to 0.3, 0.5, 0.7, and 0.9 for DS1, DS2, DS3, and collapse. The results show that

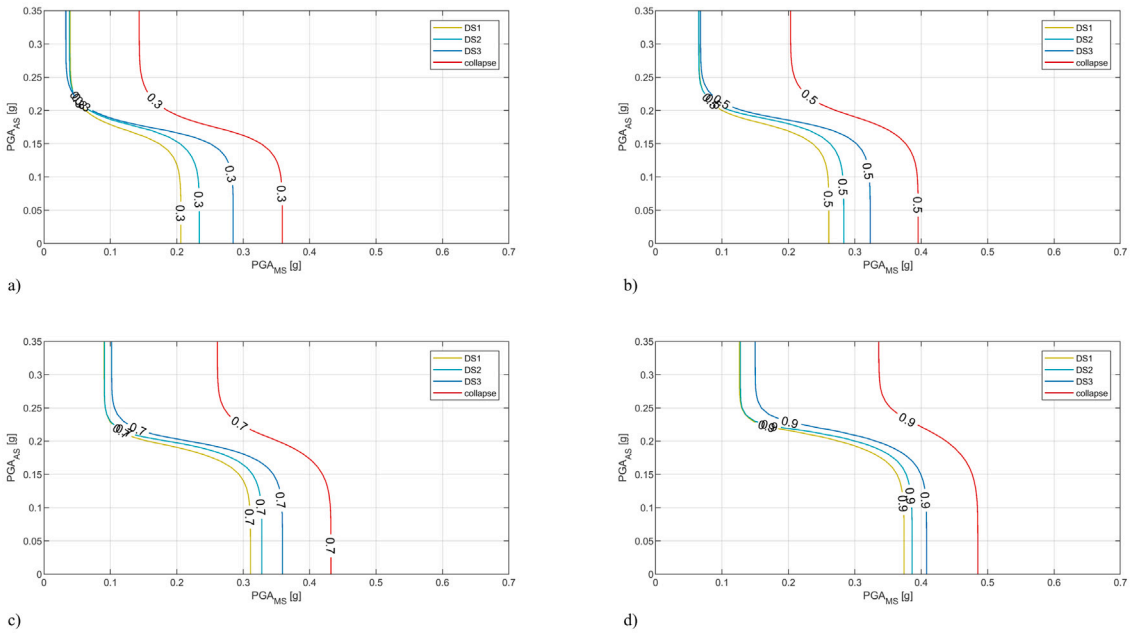

Fig. 10. Contours of the proposed fragility surfaces for DS1, DS2, DS3, and collapse at different exceedance probability levels: (a) 0.3, (b) 0.5, (c) 0.7, and (d) 0.9.

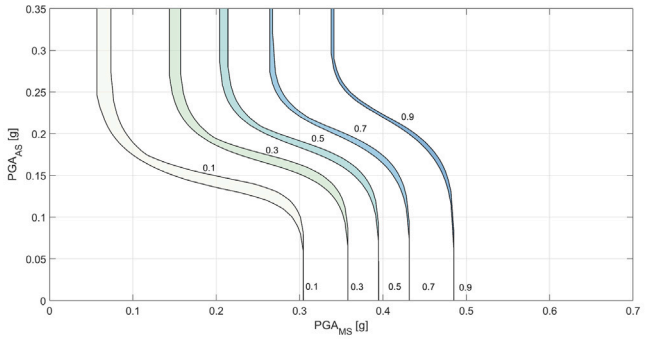

Fig. 11. Confidence bands for fragility surface contours of collapse limit state.

the expected ordering of the fragility surfaces is preserved over most of the investigated PGA_{MS}-PGA_{AS} domain. A localized crossing is observed only for the lowest probability level 0.3 in a narrow region where the contours associated with adjacent damage states nearly overlap. This crossing indicates a minor statistical inconsistency of the independently fitted fragility surfaces. Although this inconsistency is limited and does not alter the main trends discussed above, this issue arising from the adopted probabilistic fitting strategy could be addressed in future work through constrained statistical fitting techniques that explicitly enforce monotonicity among damage-state exceedance probabilities. Nevertheless, the results remain physically interpretable and confirm the increased vulnerability of structures subjected to sequential MS–AS events.

3.5. Sensitivity to strength reduction factors

The influence of the adopted strength-reduction factors on the resulting fragility assessment was examined by varying λ_Q within the ranges proposed in [62] for moderate (λ_Q = 0.6–0.8) and heavy (λ_Q = 0.4–0.6) DSs of typical masonry buildings in many European countries. The parametric analysis shows that the resulting fragility surfaces are only marginally affected by these variations. In particular, the shape and orientation of the surfaces remain essentially unchanged, and the shifts in median capacity fall well within the expected modeling uncertainty. This indicates that the proposed fragility formulation can be considered robust with respect to plausible variations in the assumed strength-reduction factors. An example of the limited impact on the collapse limit state is illustrated in Fig. 11, where confidence bands are shown for the surface contours.

It should be noted that the proposed fragility surfaces may underestimate the probability of severe damage or collapse for building typologies prone to out-of-plane mechanisms, as EPUSH software does not explicitly account for this response of the structural system. This assumption may represent a limitation for URM buildings characterized by flexible diaphragms, such as timber floors, where poor wall-to-diaphragm connections can activate out-of-plane failure modes. In such cases, out-of-plane collapse mechanisms may govern the structural response, particularly under seismic sequences, where cumulative damage and degradation of connections can exacerbate the interaction between in-plane and out-of-plane behavior. Therefore, the applicability of the proposed approach is primarily limited to URM buildings with sufficient box-like behavior, where diaphragms can ensure adequate load redistribution and prevent premature out-of-plane failure. These include, for instance, buildings with stiff or well-connected diaphragms (e.g., RC slabs), effective wall-to-floor connections, regular layouts with adequate interlocking between orthogonal walls. For buildings with flexible diaphragms or known vulnerability to out-of-plane mechanisms, the proposed methodology should be applied with caution, and may require integration with additional modeling strategies capable of capturing out-of-plane response or combined in-plane/out-of-plane interaction effects.

Finally, by quantifying the probability of reaching each DS given a sequence of two events, these surfaces can be used in loss modeling (e.g. as part of event-based or scenario-based risk analyses). They help capture cumulative damage effects instead of relying on single-event fragility.

Building on the previously discussed fragility surfaces, the bivariate cumulative distribution function of the MDR given PGA_{MS} and PGA_{AS} computed according to Eq. (15), further emphasizes how cumulative seismic demand across multiple events can have a considerable impact on collapse risk, which is hardly captured by conventional single-event loss models. Fig. 9(b), depicting the bivariate vulnerability surface for the case study, reveals that the probability of exceeding a certain level of MDR grows significantly as the intensity of the MS and AS jointly increase. Importantly, the steepness of the CDF in the direction of increasing PGA_{AS} highlights the substantial role that an AS can play in driving up the expected damage even after a low to moderate MS. This behavior is especially evident in the mid-to-high damage range, where relatively modest AS intensities can produce significant increases in MDR. Hence, this surface underscores the strong compound effects of earthquake sequences on structural performance, an aspect that is overlooked when using traditional single-event damage assessments.

Beyond these direct considerations related to the MDR surface to estimate economic losses, providing a probabilistic distribution of damage that reflects ground motion variability, they could also inform practical decision-making. For example, MDR surfaces could be incorporated into pre-screening tools that help stakeholders – such as property owners, insurers, or policy makers – evaluate expected losses under sequence-type events more realistically. Even though this study concentrates on a single structure, the methodology is broadly applicable. In portfolio or insurance applications, MDRs can help segment risks across a population of assets or integrate into loss models for earthquake-prone regions. This would enhance loss estimation procedures and facilitate more informed underwriting or resilience-focused decisions, especially when AS effects play a significant role in overall seismic risk [33,71].

4. Conclusions

Recent catastrophic events have shown how current risk models based solely on individual mainshock events are often inadequate in capturing the fragility of structures that have already been damaged due to preceding ground motions. The importance of accounting for the pre-existing damage states (DSs) in the seismic fragility analysis is particularly relevant for vulnerable structures, such as historical unreinforced masonry (URM) buildings.

This study presents a methodology for evaluating the fragility of URM structures under seismic sequences, based on vector-valued pushover analyses conditioned on mainshock (MS) and aftershock (AS) intensity levels. In the proposed framework, the probability of exceeding a given damage state is expressed as a function of the intensity measures associated with the events in the sequence. For each sequence, the structural model is updated according to the damage level reached by individual structural elements at the performance point, and the response to the AS is evaluated on the corresponding updated global capacity curve.

The application to an archetype masonry building shows that the proposed methodology can capture the evolution of damage during MS–AS sequences. The resulting vector-valued fragility model is defined in the joint space of the adopted intensity measures. In the present two-event formulation, this leads to fragility surfaces conditioned on PGA_{MS} and PGA_{AS}, which provide a direct representation of the combined effect of the MS and AS intensity levels on structural damage probability.

Despite the promising results, some limitations should be acknowledged. First, damage accumulation is not explicitly modeled in a cumulative mechanics-based sense, e.g., accounting for the full hysteretic response of the URM walls under ground motion sequences, via computationally demanding NLTHA to explicitly map stiffness and strength degradation. Damage is instead implicitly captured through the sequential update of the backbone curve at the performance point level through simplified factors from FEMA that emulate the condition of an already-damaged structure by reducing the stiffness, strength, and displacement capacity of the individual walls. Although these simplified factors are highly uncertain and rely on expert judgment, they remain consistent with the simplified nature of the proposed framework. Moreover, the parametric study indicates that their influence on the resulting fragility surfaces is limited, and the comparison with NLTHA shows that the proposed method provides demand estimates broadly consistent with those obtained from dynamic analyses based on the same equivalent-SDOF idealization. Second, the choice of alternative IMs to the PGA, adopted in this work, e.g., the *AvgSa*, may be more appropriate to URM structures exhibiting stiffness degradation and period elongation, and should be investigated in future studies. Third, the use of the Capacity Spectrum Method, while computationally efficient and widely adopted for vulnerability assessments, remains an approximate procedure that has been primarily validated for frame structures and may introduce additional epistemic uncertainty when applied to load-bearing URM

systems. Finally, since the fragility surfaces associated with the different damage states were fitted independently, a limited crossing between adjacent fragility surfaces was observed at low exceedance probability levels in a narrow region of the intensity-measure domain. Although this localized inconsistency has a limited influence on the main results, it represents a statistical limitation of the adopted fitting strategy, since higher damage states should not exhibit larger exceedance probabilities than lower damage states for the same intensity-measure pair. Further developments should therefore investigate constrained fitting procedures capable of explicitly enforcing monotonicity among damage-state exceedance probabilities.

Future research could also focus on the inclusion of epistemic uncertainties in masonry mechanical parameters within the derivation of vector-valued MS–AS fragility surfaces, on the validation of the proposed framework against refined nonlinear MDOF models and/or experimental evidence, and on its extension to real building portfolios.

CRediT authorship contribution statement

Filippo Landi: Writing – review & editing, Writing – original draft, Visualization, Validation, Supervision, Software, Methodology, Investigation, Formal analysis, Data curation, Conceptualization. **Giada Bartolini:** Writing – review & editing, Writing – original draft, Visualization, Validation, Software, Methodology, Investigation, Formal analysis, Data curation, Conceptualization. **Giacomo Sevieri:** Writing – review & editing, Software, Methodology, Data curation, Conceptualization. **Marco Baiguera:** Writing – review & editing, Methodology, Conceptualization.

Declaration of competing interest

The authors declare that they have no known competing financial interests or personal relationships that could have appeared to influence the work reported in this paper.

Data availability

Data will be made available on request.

References

[1] M. Orlacchio, G. Baltzopoulos, I. Iervolino, Simplified state-dependent seismic fragility assessment, Earthq. Eng. Struct. Dyn. 53 (6) (2024) 2099–2121, http://dx.doi.org/10.1002/eqe.4105.
[2] D.E. Goldberg, T. Taymaz, N.G. Reitman, A.E. Hatem, S. Yolsal-Çevikbilen, W.D. Barnhart, T.S. Irmak, D.J. Wald, T. Öcalan, W.L. Yeck, et al., Rapid characterization of the February 2023 Kahramanmaraş, Türkiye, earthquake sequence, Seism. Rec. 3 (2) (2023) 156–167, http://dx.doi.org/10.1785/0320230009.
[3] M. Lörinc, O. Hotový, Global catastrophe recap: First half of 2023, 2023, URL https://assets.aon.com/-/media/files/aon/capabilities/reinsurance/global-catastrophe-recap-1h-2023.pdf. (Accessed 29 October 2023).
[4] E. Damcı, R. Temür, Z. Kanbir, Ç. Şekerci, E.Ö. Köroğlu, Comprehensive investigation of damage due to 2023 Kahramanmaraş earthquakes in Türkiye: Causes, consequences, and mitigation, J. Build. Eng. 99 (2025) 111420, http://dx.doi.org/10.1016/j.jobe.2024.111420.
[5] W.Y. Kam, S. Pampanin, K. Elwood, et al., Seismic performance of reinforced concrete buildings in the 22 February Christchurch (Lyttleton) earthquake, Bull. N. Z. Soc. Earthq. Eng. 4 (44) (2012) 239–279, http://dx.doi.org/10.5459/bnzsee.44.4.239-278.
[6] A. Sextos, R. De Risi, A. Pagliaroli, S. Foti, F. Passeri, E. Ausilio, R. Cairo, M.C. Capatti, F. Chiabrando, A. Chiaradonna, et al., Local site effects and incremental damage of buildings during the 2016 central Italy earthquake sequence, Earthq. Spectra 34 (4) (2018) 1639–1669, http://dx.doi.org/10.1193/100317EQS194M.
[7] R. Sisti, M. Di Ludovico, A. Borri, A. Prota, Damage assessment and the effectiveness of prevention: the response of ordinary unreinforced masonry buildings in Norcia during the central Italy 2016–2017 seismic sequence, Bull. Earthq. Eng. 17 (2019) 5609–5629, http://dx.doi.org/10.1007/s10518-018-0448-z.
[8] W. Marzocchi, M. Taroni, Some thoughts on declustering in probabilistic seismic-hazard analysis, Bull. Seismol. Soc. Am. 104 (4) (2014) 1838–1845, http://dx.doi.org/10.1785/0120130300.
[9] A.N. Papadopoulos, P. Bazzurro, W. Marzocchi, Exploring probabilistic seismic risk assessment accounting for seismicity clustering and damage accumulation: Part I. Hazard analysis, Earthq. Spectra 37 (2) (2021) 803–826, http://dx.doi.org/10.1177/8755293020957338.
[10] P. Bazzurro, C. Cornell, C. Menun, M. Motahari, Guidelines for seismic assessment of damaged buildings, in: 13th World Conference on Earthquake Engineering, Vol. 1708, 2004.
[11] M.C. Gerstenberger, W. Marzocchi, T. Allen, M. Pagani, J. Adams, L. Danciu, E.H. Field, H. Fujiwara, N. Luco, K.-F. Ma, et al., Probabilistic seismic hazard analysis at regional and national scales: State of the art and future challenges, Rev. Geophys. 58 (2) (2020) e2019RG000653, http://dx.doi.org/10.1029/2019RG000653.
[12] M. Orlacchio, E. Chioccarelli, I. Iervolino, State-dependent fragility functions for Italian building classes, Soil Dyn. Earthq. Eng. 182 (2024) 108685, http://dx.doi.org/10.1016/j.soildyn.2024.108685.
[13] I. Iervolino, E. Chioccarelli, A. Suzuki, Seismic damage accumulation in multiple mainshock–aftershock sequences, Earthq. Eng. Struct. Dyn. 49 (10) (2020) 1007–1027, http://dx.doi.org/10.1002/eqe.3275.
[14] J. Ruiz-García, J.D. Aguilar, Aftershock seismic assessment taking into account postmainshock residual drifts, Earthq. Eng. Struct. Dyn. 44 (9) (2015) 1391–1407, http://dx.doi.org/10.1002/eqe.2523.
[15] F. Jalayer, H. Ebrahimian, A. Miano, G. Manfredi, H. Sezen, Analytical fragility assessment using unscaled ground motion records, Earthq. Eng. Struct. Dyn. 46 (15) (2017) 2639–2663, http://dx.doi.org/10.1002/eqe.2922.
[16] J.-S. Jeon, R. DesRoches, L.N. Lowes, I. Brilakis, Framework of aftershock fragility assessment–case studies: older California reinforced concrete building frames, Earthq. Eng. Struct. Dyn. 44 (15) (2015) 2617–2636, http://dx.doi.org/10.1002/eqe.2599.
[17] K. Aljawhari, R. Gentile, F. Freddi, C. Galasso, Effects of ground-motion sequences on fragility and vulnerability of case-study reinforced concrete frames, Bull. Earthq. Eng. 19 (2021) 6329–6359, http://dx.doi.org/10.1007/s10518-020-01006-8.
[18] M. Polese, M. Di Ludovico, A. Prota, G. Manfredi, et al., Residual capacity of earthquake damaged buildings, in: Proceedings of the 15th World Conference on Earthquake Engineering, Lisboa, Portugal, 2012.

[19] M. Polese, M. Di Ludovico, A. Prota, G. Manfredi, Damage-dependent vulnerability curves for existing buildings, Earthq. Eng. Struct. Dyn. 42 (6) (2013) 853–870, http://dx.doi.org/10.1002/eqe.2249.
[20] L. Pedone, R. Gentile, C. Galasso, S. Pampanin, Nonlinear static procedures for state-dependent seismic fragility analysis of reinforced concrete buildings, in: Fib Symposium, Vol. 56, fib: The International Federation for Structural Concrete, 2021, pp. 47–54.
[21] A. Nettis, R. Gentile, D. Raffaele, G. Uva, C. Galasso, Cloud capacity spectrum method: Accounting for record-to-record variability in fragility analysis using nonlinear static procedures, Soil Dyn. Earthq. Eng. 150 (2021) 106829, http://dx.doi.org/10.1016/j.soildyn.2021.106829.
[22] G. Rinaldin, C. Amadio, M. Fragiacomo, A component approach for the hysteretic behaviour of connections in cross-laminated wooden structures, Earthq. Eng. Struct. Dyn. 42 (13) (2013) 2023–2042, http://dx.doi.org/10.1002/eqe.2310.
[23] P.G.d. Inarritu, M. Kohrangi, S. Cattari, S. Lagomarsino, P. Bazzurro, Considering cumulative damage in URM buildings for clustered seismicity risk assessment, Earthq. Eng. Struct. Dyn. 54 (4) (2025) 1172–1190, http://dx.doi.org/10.1002/eqe.4304.
[24] X. Yu, Z. Zhou, W. Du, D. Lu, Development of fragility surfaces for reinforced concrete buildings under mainshock-aftershock sequences, Earthq. Eng. Struct. Dyn. 50 (15) (2021) 3981–4000, http://dx.doi.org/10.1002/eqe.3542.
[25] M. Harati, J.W. van de Lindt, Mainshock-aftershock fragility surfaces: A machine learning approach using direct successive simulation, Int. J. Disaster Risk Reduct. 118 (2025) 105886, http://dx.doi.org/10.1016/j.ijdrr.2025.105886.
[26] P.G.d. Inarritu, M. Kohrangi, P. Bazzurro, Damage assessment of unreinforced masonry buildings incorporating damage accumulation, Earthq. Eng. Struct. Dyn. 53 (6) (2024) 2122–2140, http://dx.doi.org/10.1002/eqe.4106.
[27] ISTAT - Istituto Nazionale di Statistica, Censimento della popolazione e delle abitazioni, 2025, http://dati-censimentopopolazione.istat.it. (Accessed 07 April 2025).
[28] K. Goda, R. De Risi, Future perspectives of earthquake-tsunami catastrophe modelling: From single-hazards to cascading and compounding multi-hazards, Front. Built Environ. 8 (2023) 1022736, http://dx.doi.org/10.3389/fbuil.2022.1022736.
[29] K. Mitchell-Wallace, M. Jones, J. Hillier, M. Foote, Natural Catastrophe Risk Management and Modelling: A Practitioner's Guide, John Wiley & Sons, 2017.
[30] L. Pedone, R. Gentile, C. Galasso, S. Pampanin, Energy-based procedures for seismic fragility analysis of mainshock-damaged buildings, Front. Built Environ. 9 (2023) 1183699, http://dx.doi.org/10.3389/fbuil.2023.1183699.
[31] F. Parisse, S. Cattari, R. Marques, P. Lourenço, G. Magenes, K. Beyer, B. Calderoni, G. Camata, E. Cordasco, M. Erberik, et al., Benchmarking the seismic assessment of unreinforced masonry buildings from a blind prediction test, in: Structures, Vol. 31, Elsevier, 2021, pp. 982–1005, http://dx.doi.org/10.1016/j.istruc.2021.01.096.
[32] G. Magenes, P. Lourenço, S. Cattari, Special session 18: Seismic modeling of masonry buildings: Present knowledge and open challenges for research and practice, in: Proceedings of the 16th European Conference on Earthquake Engineering, Thessaloniki, Greece, 2018, pp. 18–21.
[33] L. Martins, V. Silva, Development of a fragility and vulnerability model for global seismic risk analyses, Bull. Earthq. Eng. 19 (15) (2021) 6719–6745, http://dx.doi.org/10.1007/s10518-020-00885-1.
[34] S.K. Ramamoorthy, P. Gardoni, J.M. Bracci, Probabilistic demand models and fragility curves for reinforced concrete frames, J. Struct. Eng. 132 (10) (2006) 1563–1572, http://dx.doi.org/10.1061/(ASCE)0733-9445(2006)132:10(1563).
[35] G.D. Hatzigeorgiou, D.E. Beskos, Inelastic displacement ratios for SDOF structures subjected to repeated earthquakes, Eng. Struct. 31 (11) (2009) 2744–2755, http://dx.doi.org/10.1016/j.engstruct.2009.07.002.
[36] S. Veismoradi, A. Cheraghi, E. Darvishan, Probabilistic mainshock-aftershock collapse risk assessment of buckling restrained braced frames, Soil Dyn. Earthq. Eng. 115 (2018) 205–216, http://dx.doi.org/10.1016/j.soildyn.2018.08.029.
[37] R. Gentile, C. Galasso, Hysteretic energy-based state-dependent fragility for ground-motion sequences, Earthq. Eng. Struct. Dyn. 50 (4) (2021) 1187–1203, http://dx.doi.org/10.1002/eqe.3387.
[38] P.G.d. Inarritu, M. Kohrangi, S. Cattari, S. Lagomarsino, P. Bazzurro, Considering cumulative damage in URM buildings for clustered seismicity risk assessment, Earthq. Eng. Struct. Dyn. 54 (4) (2025) 1172–1190, http://dx.doi.org/10.1002/eqe.4304.
[39] H. Dávalos, E. Miranda, Filtered incremental velocity: A novel approach in intensity measures for seismic collapse estimation, Earthq. Eng. Struct. Dyn. 48 (12) (2019) 1384–1405, http://dx.doi.org/10.1002/eqe.3205.
[40] G.J. O'Reilly, Limitations of Sa (T 1) as an intensity measure when assessing non-ductile infilled RC frame structures, Bull. Earthq. Eng. 19 (6) (2021) 2389–2417, http://dx.doi.org/10.1007/s10518-021-01086-0.
[41] M. Ciano, M. Gioffre, M. Grigoriu, The role of intensity measures on the accuracy of seismic fragilities, Probabilistic Eng. Mech. 60 (2020) 103041, http://dx.doi.org/10.1016/j.probengmech.2020.103041.
[42] M. Nale, F. Minghini, A. Chiozzi, A. Tralli, Fragility functions for local failure mechanisms in unreinforced masonry buildings: a typological study in Ferrara, Italy, Bull. Earthq. Eng. 19 (14) (2021) 6049–6079, http://dx.doi.org/10.1007/s10518-021-01199-6.
[43] N. Buratti, F. Minghini, E. Ongaretto, M. Savoia, N. Tullini, Empirical seismic fragility for the precast RC industrial buildings damaged by the 2012 Emilia (Italy) earthquakes, Earthq. Eng. Struct. Dyn. 46 (14) (2017) 2317–2335, http://dx.doi.org/10.1002/eqe.2906.
[44] Italian Public Works Council, Memorandum for Application of Italian Building Code, N. 7, Istituto Poligrafico e Zecca dello Stato, Rome, Italy, 2019, (In Italian).
[45] S. Lagomarsino, S. Giovinazzi, Macroseismic and mechanical models for the vulnerability and damage assessment of current buildings, Bull. Earthq. Eng. 4 (2006) 415–443, http://dx.doi.org/10.1007/s10518-006-9024-z.
[46] I.M. Franco, C. Smerzini, A. Rosti, M. Rota, R. Paolucci, A. Penna, Seismic fragility curves with unconventional ground motion intensity measures from physics-based simulations, Bull. Earthq. Eng. 23 (5) (2025) 1885–1915, http://dx.doi.org/10.1007/s10518-025-02104-1.
[47] M. Rota, A. Penna, G. Magenes, A methodology for deriving analytical fragility curves for masonry buildings based on stochastic nonlinear analyses, Eng. Struct. 32 (5) (2010) 1312–1323, http://dx.doi.org/10.1016/j.engstruct.2010.01.009.
[48] G. Sevieri, R. Gentile, C. Galasso, A multi-fidelity Bayesian framework for robust seismic fragility analysis, Earthq. Eng. Struct. Dyn. 50 (15) (2021) 4199–4219, http://dx.doi.org/10.1002/eqe.3552.
[49] K. Goda, C.A. Taylor, Effects of aftershocks on peak ductility demand due to strong ground motion records from shallow crustal earthquakes, Earthq. Eng. Struct. Dyn. 41 (15) (2012) 2311–2330, http://dx.doi.org/10.1002/eqe.2188.
[50] K. Goda, F. Wenzel, R. De Risi, Empirical assessment of non-linear seismic demand of mainshock–aftershock ground-motion sequences for Japanese earthquakes, Front. Built Environ. 1 (2015) 6, http://dx.doi.org/10.3389/fbuil.2015.00006.
[51] K. Goda, G. Campbell, L. Hulme, B. Ismael, L. Ke, R. Marsh, P. Sammonds, E. So, Y. Okumura, N. Kishi, et al., The 2016 Kumamoto earthquakes: cascading geological hazards and compounding risks, Front. Built Environ. 2 (2016) 19, http://dx.doi.org/10.3389/fbuil.2016.00019.
[52] S. Iacoletti, G. Cremen, C. Galasso, Modeling damage accumulation during ground-motion sequences for portfolio seismic loss assessments, Soil Dyn. Earthq. Eng. 168 (2023) 107821, http://dx.doi.org/10.1016/j.soildyn.2023.107821.
[53] M. Akhani, N. Alidadi, S. Pezeshk, Application of metaheuristic algorithms in ground motion selection and scaling for time history analysis of structures, J. Struct. Eng. 150 (8) (2024) 04024094, http://dx.doi.org/10.1061/JSENDH.STENG-13470.
[54] P. Croce, F. Landi, P. Formichi, Probabilistic seismic assessment of existing masonry buildings, Buildings 9 (12) (2019) 237, http://dx.doi.org/10.3390/buildings9120237.
[55] M.L. Beconcini, P. Formichi, L. Giresini, F. Landi, B. Puccini, P. Croce, Modeling approaches for the assessment of seismic vulnerability of masonry structures: The E-PUSH program, Buildings 12 (3) (2022) 346, http://dx.doi.org/10.3390/buildings12030346.

[56] P. Fajfar, A nonlinear analysis method for performance-based seismic design, Earthq. Spectra 16 (3) (2000) 573–592, http://dx.doi.org/10.1193/1.1586128.
[57] S.A. Freeman, Review of the development of the capacity spectrum method, ISET J. Earthq. Technol. 41 (1) (2004) 1–13.
[58] F. Landi, E-PUSH software version 5.0, 2021, http://dx.doi.org/10.13140/RG.2.2.34797.97767.
[59] F. Landi, N. Friedman, G. Bartolini, B. Popovics, A. Friedman, Bimquake, 2026, http://dx.doi.org/10.5281/zenodo.18510523.
[60] P. Fajfar, Capacity spectrum method based on inelastic demand spectra, Earthq. Eng. Struct. Dyn. 28 (9) (1999) 979–993, http://dx.doi.org/10.1002/(SICI)1096-9845(199909)28:9<979::AID-EQE850>3.0.CO;2.
[61] Applied Technology Council, Evaluation of Earthquake Damaged Concrete and Masonry Wall Buildings, Basic Procedure Manual (FEMA 306), Tech. Rep., Federal Emergency Management Agency, Washington, D.C., 1998.
[62] S. Lagomarsino, D. Camilletti, S. Cattari, S. Marino, Seismic assessment of existing irregular masonry buildings by nonlinear static and dynamic analyses, in: European Conference on Earthquake Engineering Thessaloniki, Greece, Springer, 2018, pp. 123–151.
[63] K.V. Mardia, Measures of multivariate skewness and kurtosis with applications, Biometrika 57 (3) (1970) 519–530, http://dx.doi.org/10.1093/biomet/57.3.519.
[64] M. Dolce, A. Prota, B. Borzi, F. da Porto, S. Lagomarsino, G. Magenes, C. Moroni, A. Penna, M. Polese, E. Speranza, et al., Seismic risk assessment of residential buildings in Italy, Bull. Earthq. Eng. 19 (2021) 2999–3032, http://dx.doi.org/10.1007/s10518-020-01009-5.
[65] Federal Emergency Management Agency, HAZUS Earthquake Model Technical Manual, Tech. Rep. Version 2.1, Federal Emergency Management Agency (FEMA), 2020, URL . (Accessed 22 May 2025-05-22).
[66] F. Graziotti, A. Penna, G. Magenes, A nonlinear SDOF model for the simplified evaluation of the displacement demand of low-rise URM buildings, Bull. Earthq. Eng. 14 (6) (2016) 1589–1612, http://dx.doi.org/10.1007/s10518-016-9896-5.
[67] G. Guerrini, F. Graziotti, A. Penna, G. Magenes, Improved evaluation of inelastic displacement demands for short-period masonry structures, Earthq. Eng. Struct. Dyn. 46 (9) (2017) 1411–1430, http://dx.doi.org/10.1002/eqe.2862.
[68] R. Gentile, C. Galasso, Simplicity versus accuracy trade-off in estimating seismic fragility of existing reinforced concrete buildings, Soil Dyn. Earthq. Eng. 144 (2021) 106678, http://dx.doi.org/10.1016/j.soildyn.2021.106678.
[69] R.A. Johnson, D.W. Wichern, Applied Multivariate Statistical Analysis, Sixth ed., Pearson Prentice Hall, Upper Saddle River, NJ, 2007.
[70] FEMA, HAZUS-MH Technical Manual: Earthquake Model, Federal Emergency Management Agency, Washington, D.C., USA, 2010, Multi-hazard loss estimation methodology.
[71] L. Sousa, V. Silva, M. Marques, H. Crowley, On the treatment of uncertainty in seismic vulnerability and portfolio risk assessment, Earthq. Eng. Struct. Dyn. 47 (1) (2018) 87–104, http://dx.doi.org/10.1002/eqe.2940.